REPORT DOCUMENTATION PAGE

Form Approved OMB No. 0704-0188

1. REPORT DATE (DD-MM-YYYY) 01-12-2006	2. REPORT TYPE Final Report	3. DATES COVERED (From – To) 1 May 2004 - 24-Jun-09

4. TITLE AND SUBTITLE

Feedback control and estimation applied to boundary layers subjected to free-stream turbulence.

5a. CONTRACT NUMBER
FA8655-04-1-3032

5b. GRANT NUMBER

5c. PROGRAM ELEMENT NUMBER

6. AUTHOR(S)

Professor Dan S Henningson

5d. PROJECT NUMBER

5d. TASK NUMBER

5e. WORK UNIT NUMBER

7. PERFORMING ORGANIZATION NAME(S) AND ADDRESS(ES)
KTH The Royal Institute of Technology
Stockholm S-100 44
Sweden

8. PERFORMING ORGANIZATION REPORT NUMBER

N/A

9. SPONSORING/MONITORING AGENCY NAME(S) AND ADDRESS(ES)

EOARD
Unit 4515 BOX 14
APO AE 09421

10. SPONSOR/MONITOR'S ACRONYM(S)

11. SPONSOR/MONITOR'S REPORT NUMBER(S)
Grant 04-3032

12. DISTRIBUTION/AVAILABILITY STATEMENT

Approved for public release; distribution is unlimited.

13. SUPPLEMENTARY NOTES

14. ABSTRACT

This report results from a contract tasking KTH The Royal Institute of Technology as follows: The grantee will investigate and develop linear feedback control and estimation techniques for nonlinear wall-bounded transitional and turbulent flow phenomena, and to apply them in numerical closed-loop flow simulations. Control will be applied through blowing and suction at the wall to manage transition in boundary layers exposed to high levels of free-stream turbulence. Specifically, an estimation technique and full-state feedback control will be combined to compensate based upon wall information. To achieve this, full information feedback control will first be implemented in the numerical simulation of a spatially evolving boundary layer exposed to free-stream turbulence. Controller parameters will then be tuned in order to maximize performance. An estimation technique will then be implemented using an extended Kalman filter, and this will be tuned for performance as well. Finally, the controller and estimator will be combined, and the performance of the resulting output feedback compensator will be compared to that of the full information control. This approach represents a step forward in the applicability and realization of linear feedback control for realistic nonlinear control situations.

15. SUBJECT TERMS
EOARD, Flow Control, Boundary Layer, Turbine Blade Cooling, Turbine Blade , Turbulence

16. SECURITY CLASSIFICATION OF:			17. LIMITATION OF ABSTRACT UL	18, NUMBER OF PAGES	19a. NAME OF RESPONSIBLE PERSON SURYA SURAMPUDI
a. REPORT UNCLAS	b. ABSTRACT UNCLAS	c. THIS PAGE UNCLAS		26	19b. TELEPHONE NUMBER (Include area code) +44 (0)1895 616021

Standard Form 298 (Rev. 8/98)
Prescribed by ANSI Std. Z39-18

Feedback control and estimation applied to boundary layers subject to free-stream turbulence

Philipp Schlatter, Jérôme Hœpffner, Luca Brandt,
Espen Åkervik, and Dan S. Henningson
Department of Mechanics, KTH, Stockholm

2006-11-01

1   Introduction

The present report concerns PHASE 3 of the EOARD project with grant no. 043032. The controller was seen to work adequately, as reported in the comprehensive report on PHASE 1, and during PHASE 2 we mainly concentrated on analyzing, implementing and testing the estimator, as reported in the comprehensive report of PHASE 2.

This comprehensive report on PHASE 3 includes the introductory sections from the report of PHASE 1 so that it can be read without direct reference to the older report, i.e. sections 2 and 3 in the present report. It also includes summaries of the report on PHASE 2, i.e sections 4 and 5 in the present report. The main new material in this report is included in section 6, where we have implemented and used LES (Large-Eddy Simulations) methodology for simulation and control of free-stream turbulence. This was not included in the original proposal, but was deemed necessary since the simulations were quite time consuming. We have found a very good LES model which captures all of the physics but reduces the computational cost to about 1% of the full Direct Numerical Simulations. One can also in the future use the LES methodology just for the estimation simulations and thus view it as a form of a model reduction.

In PHASE 3 Dr. Luca Brandt, Dr. Philipp Schlatter and Espen Åkervik have been involved in the estimation and control simulations reported in section 6, including the LES implementation and simulations. Prof. Dan Henningson is the project leader. The funding for PHASE 3, 40.000 USD, has mainly been used to partially cover the salaries of Philipp Schlatter and Luca Brandt.

2 Simulation of transition in boundary layers subject to free-stream turbulence

Transition to turbulence in a boundary layer subject to free-stream turbulence is of a great technological importance in many applications. Under free-stream turbulence intensities of 1% or more it is observed experimentally [1] that transition occurs rapidly, bypassing the scenario triggered by unstable Tollmien-Schlichting waves. In the bypass transition scenario, low frequency oscillations, associated with long streaky structures in the streamwise velocity component appear. The initial amplification of these structures can be explained by non-modal growth theory [2]. As the streaks reach a threshold amplitude, they undergo a secondary instability before a breakdown to turbulence occurs in the form of localized turbulent spots (see, for example, [4, 5]).

2.1 Numerical method

The direct numerical simulations presented here have all been performed with the pseudo-spectral algorithm described in [6]. The numerical code used solves the three-dimensional, time-dependent, incompressible Navier-Stokes equations. The algorithm uses Fourier representation in the streamwise and spanwise directions and Chebyshev polynomials in the wall-normal direction, together with a pseudo-spectral treatment of the nonlinear terms. The time advancement used is a four-step low-storage third-order Runge–Kutta method for the nonlinear terms and a second-order Crank–Nicolson method for the linear terms. Aliasing errors from the evaluation of the nonlinear terms are removed by the $\frac{3}{2}$-rule when the FFTs are calculated in the wall parallel plane.

To correctly account for the downstream boundary layer growth a spatial technique is necessary. This requirement is combined with the periodic boundary condition in the streamwise direction by the implementation of a "fringe region", similar to that described by [7]. In this region, at the downstream end of the computational box, the function $\lambda(x)$ in equation (1) is smoothly raised from zero and the flow is forced to a desired solution v in the following manner,

$$\frac{\partial u}{\partial t} = NS(u) + \lambda(x)(v - u) + g, \tag{1}$$

$$\nabla \cdot u = 0, \tag{2}$$

where u is the solution vector and $NS(u)$ the right hand side of the (unforced) momentum equations. Both g, which is a disturbance forcing, and v may depend on the three spatial coordinates and time. The forcing vector v is smoothly changed from the laminar boundary layer profile at the beginning of the fringe region to the prescribed inflow velocity vector. This method damps disturbances flowing out of the physical region and smoothly transforms the flow to the desired inflow state, with a minimal upstream influence (see [8] for an investigation of the fringe region technique).

2.2 Free-stream turbulence generation

Using this numerical code, disturbances can be introduced in the laminar flow by including them in the flow field v, thereby forcing them in the fringe region. Following [9], a turbulent inflow is described as a superposition of modes of the continuous spectrum of the linearized Orr-Sommerfeld and Squire operators. These modes have been added to the forcing vector v. Isotropic grid turbulence can be reproduced by a sum of Fourier modes with random amplitudes [10]; however in the presence of an inhomogeneous direction an alternative complete basis is required; in particular, in the present case, the new basis functions need to accommodate the wall. A natural choice is therefore the use of the modes of the continuous spectrum [11]. A three-dimensional wave-vector $\kappa = (\alpha, \gamma, \beta)$ c an be associated to each eigenfunction of the continuous spectrum: The streamwise and spanwise wave numbers α and β are defined by the normal mode expansion in the homogeneous directions of the underlying linear problem while the wall-normal wavelength is determined by the eigenvalue along the continuous spectrum. Invoking Taylor's hypothesis, the streamwise wavenumber α can be replaced by a frequency $\omega = \alpha U_\infty$ and the expansion may be written

$$u = \sum A_N \, \hat{u}_N(y) \, e^{(i\beta z + i\alpha x - i\omega t)},$$

where the real values of β and ω and the complex wavenumber α are selected according to the procedure described below. Note that the desired wall-normal wavenumber γ enters through the eigenfunction shape $\hat{u}_N(y)$ and it is defined by the eigenvalue α. In particular, the wave numbers pertaining to the modes used in the expansion are selected by defining in the wavenumber space (ω, γ, β) a number of spherical shells of radius $|\kappa|$. 40 points are then placed randomly but at equal intervals on the surface of these spheres. The amplitude $|A_N|$ is in fact the same for all modes on each shell and reproduces the following analytical expression for a typical energy spectrum of homogeneous isotropic turbulence

$$E(\kappa) = \frac{2}{3} \frac{a \, (\kappa L)^4}{(b + (\kappa L)^2)^{17/6}} L \, Tu. \tag{3}$$

In the expression above, Tu is the turbulence intensity, L a characteristic integral length scale and a, b two normalization constants. The methodology briefly introduced here is able to satisfactorily reproduce a boundary layer subject to free-stream turbulence as documented in [12].

2.3 Transition scenario in boundary layers subject to free-stream turbulence

A snapshot of the flow is shown in figure 1 where the instantaneous streamwise and spanwise velocities are plotted in a plane parallel to the wall. The overall picture of the transition scenario can be deduced from the figure. Starting from the inlet position, the perturbation in the boundary layer appears mainly in the streamwise velocity component, in the form of elongated structures. Patches of irregular motion are seen to appear further
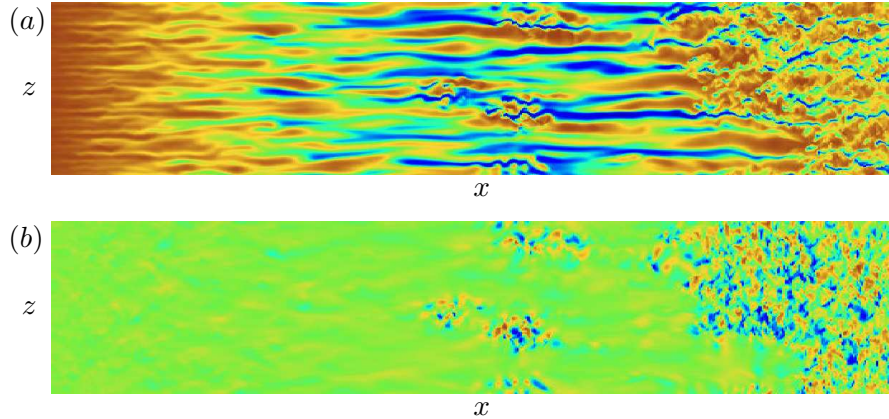
Figure 1: (a) Instantaneous streamwise velocity and (b) spanwise velocity (bottom figure) in a plane parallel to the wall at $y/\delta_0^* = 2$. The plots are not at the actual scale since the domain depicted is 900 units long and 90 units wide in terms of δ_0^*. The fringe region is not shown.

downstream; these are more evident in the spanwise component. As they travel downstream, the spots become wider and longer. Note also that laminar streaks can be observed downstream of the spots. The turbulent region at the end of the domain is created by the enlargement and merging of the various spots and therefore the streamwise position at which the flow is turbulent varies with time; the turbulent flow is convected downstream and it would not be seen if new spots were not formed all the time.

The breakdown has been analyzed in detail in [12] by looking at the instantaneous three-dimensional flow configurations for a number of spots, tracing back in time the location of their formation. An important feature of the spot precursors, observed in all cases considered, is the presence of regions of positive and negative wall-normal and spanwise velocity arranged in a quasi-periodic array. This region of perturbed flow is growing while travelling downstream in the typical manner of a wave packet. Such quasi regular distribution of the cross-stream velocity components is responsible for the observed wavy motions of the streaks preceding the breakdown. Visual inspection of many velocity fields enabled to classify the type of breakdown occurring on the streaks by considering the spanwise symmetry of the wall-normal and spanwise velocities and their position relative to the underlying streak.

The flow structures at the incipient spot stage resemble very much those observed in previous study on the breakdown of steady symmetric streaks, both in the case of the scenario following a sinuous instability, see [13], and in the case of a varicose scenario, see the experiments in [14]. The similarity with either of the two cases is observed in all spots under consideration.

3 The linear compensator

3.1 Formulation

An estimation technique and full-state feedback control can be combined to obtain a compensator based on wall information. We express the governing equations for each horizontal wavenumber pair in the form

$$\begin{cases} \dot{\psi} = A\,\psi + B_1 d + B_2 f_c, \\ r = C_2 \psi + g. \end{cases}$$

The input operator B_2 describe how the control input f_c affect the system. The measurement output r is extracted from the state variable using the measurement operator C_2 and is corrupted by the sensor noise g. In §3.1.1 and §3.1.2, we will model the external disturbances and sensor noise as stochastic processes.

3.1.1 External sources of disturbances

The performance of the state estimation relies on the construction of a proper model for the flow disturbances. Indeed, if the external sources of perturbation in the flow are well identified, it becomes an easy task to estimate the flow evolution using a dynamic model for the system.

The external sources of perturbations in typical aeronautical applications can be wall roughness, accoustic waves, and freestream turbulence. When using a linear model for the flow, the nonlinear effects can be seen as additional disturbances to the dynamic evolution. An appropriate model for the disturbances and associated covariance is essential for fast convergence of the estimator.

3.1.2 Sensors and sensor noise

The measurements used in this study are the streamwise and spanwise shear stresses and wall pressure fluctuations.

$$\begin{cases} \tau_x = \tau_{xy}|_{\text{wall}} = \dfrac{1}{Re}\left.\dfrac{\partial u}{\partial y}\right|_{\text{wall}} = \dfrac{1}{Re}\dfrac{i}{k^2}(k_x D^2 v - k_z D\eta)|_{\text{wall}}, \\[2mm] \tau_z = \tau_{zy}|_{\text{wall}} = \dfrac{1}{Re}\left.\dfrac{\partial w}{\partial y}\right|_{\text{wall}} = \dfrac{1}{Re}\dfrac{i}{k^2}(k_z D^2 v + k_x D\eta)|_{\text{wall}}, \\[2mm] p = p|_{\text{wall}} = \dfrac{1}{Re}\dfrac{1}{k^2}D^3 v|_{\text{wall}}. \end{cases}$$

Each of the three measurements is assumed to be corrupted by random sensor noise processes, the amplitude of which is determined by the assumed quality of the sensors. The covariance of the sensor noise vector g can thus be described in Fourier space by a 3×3 matrix G whose diagonal elements α_ι^2 are the variances of the sensor noise assumed to be associated with each individual sensor

$$G_{g_\iota(t),g_\kappa(t')} = \delta_{\iota\kappa}\delta(t - t')\alpha_\iota^2, \tag{4}$$

where $\delta_{\iota\kappa}$ denotes the Kronecker delta. Thus, in the present work, we assume that the sensor noise is uncorrelated in both space and time.

When the signal-to-noise ratio is low, the measured signal must be fed back only gently into the estimator, lest the sensor noise disrupt the estimator. When the signal-to-noise ratio is high, the measured signal may be fed back more aggressively into the estimator, as the fidelity of the measurements can be better trusted. For a given covariance of the external disturbances, the tuning of the assumed overall magnitude of the sensor noise in the Kalman filter design thus provides a natural "knob" to regulate the magnitude of the feedback into the estimator.

3.2 Compensation

3.2.1 Control feedback

Control is applied through blowing and suction at the wall and it is therefore introduced as a boundary condition (v_0). The boundary condition is lifted through linear super-position into the domain and the governing equations for each horizontal wavenumber pair can be expressed in the standard form,

$$\dot{x} = \mathcal{A}x + \mathcal{B}_1 d + \mathcal{B}_2 f_c, \quad x = [\boldsymbol{\psi}, \, v_0]^T, \quad f_c = \frac{\partial v_0}{\partial t},$$

If $\boldsymbol{\psi}_p$ is a stationary solution to the inhomogeneous Orr–Sommerfeld/Squire equation with $v_0 = 1$ the augmented operators can be written,

$$\mathcal{A} = \begin{bmatrix} A & 0 \\ 0 & 0 \end{bmatrix}, \mathcal{B}_1 = \begin{bmatrix} B & 0 \\ 0 & 0 \end{bmatrix}, \quad \mathcal{B}_2 = \begin{bmatrix} -\boldsymbol{\psi}_p \\ 1 \end{bmatrix}.$$

The aim is to minimize the objective function:

$$\begin{aligned} J(v_0) &= \frac{1}{2} \int_0^T \int_\Omega |\mathbf{V}|^2 \, d\Omega \, dt + \frac{\ell^2}{2} \int_0^T \int_\Gamma \left| \frac{\partial v_0}{\partial t} \right|^2 d\Gamma \, dt \\ &= \sum_{k_x, k_z} \frac{1}{2} \int_0^T (x^* \mathcal{Q} x + \ell^2 f_c{}^* f_c) \, dt, \end{aligned}$$

where $\mathbf{V}$ is the disturbance velocity vector in physical space, $\mathcal{Q}$ is a measure of the kinetic energy of the perturbation for the augmented system, and l is a parameter accounting for the cost and thus penalising the magnitude of the control f_c. An extra penalty factor r is added in the definition of the energy matrix $\mathcal{Q}$. It penalizes the kinetic energy of the velocity perturbation induced by the non-homogeneous boundary condition inside the flow (see [18]).

By letting $T \to \infty$ in the objective function the optimal controller is given by

$$f_c = \mathcal{K}x, \quad \text{where} \quad \mathcal{K} = -\frac{1}{\ell^2} \mathcal{B} \mathcal{X}$$

and $\mathcal{X}$ is the positive self-adjoint solution to the Riccati equation,

$$\mathcal{X} \mathcal{A} + \mathcal{A}^* \mathcal{X} - \mathcal{X} \frac{1}{\ell^2} \mathcal{B}_2 \mathcal{B}_2^* \mathcal{X} + \mathcal{Q} = 0.$$

3.2.2 Estimation feedback

To compute the linear optimal control from the relations above the estimated flow $\check{\psi}$ is used. This is computed as solution of the Orr–Sommerfeld/Squire system with an optimal forcing designed to minimize the difference between the flow state ψ and the estimate $\check{\psi}$. The model of the estimated flow has the form

$$\begin{cases} \dot{\check{\psi}} = A\check{\psi} + B_2 f_c - f_e, \\ \check{r} = C_2\check{\psi}, \\ f_e = L\tilde{r} = L(r - \check{r}), \end{cases}$$

where $\check{y}$ is the measurement in the estimator. An estimator forcing can be computed for each wavenumber pair as

$$L = -Y\,G^{-1}\,C_2^*,$$

where Y is the positive self-adjoint solution to the Riccati equation,

$$A^*Y + Y A - Y C_2^* G^{-1} C_2 Y + B_1 R B_1 = 0.$$

3.2.3 Extension to spatially developing flows

The compensator problem is stated for a parallel flow. In order to extend the use of the model to a spatially evolving flow two locations need to be specified, one for the control and one for the estimator, where the local velocity profiles are taken to be used in the Orr–Sommerfeld/Squire operator. The flow is then assumed to be locally parallel around these locations in order to solve the control and estimation problems.

Combining the controller and estimator results in an output feedback dynamic compensator. In this case the estimator forcing given from the linear problem is applied in nonlinear, non-parallel simulations, and this is known as an extended Kalman filter. In a numerical experiment, two velocity fields are marched simultaneously forward in time. One represents the actual flow where measurements are taken and the other the estimator in which the flow is reconstructed through the forcing L based on the measurements. The following three steps describe the compensator process. Compute the difference between the measurements from the estimator flow and the "real" flow. Compute and apply the estimator forcing to the estimated flow and then compute the control signal based on the state in the estimator. Apply the computed control signal to both the "real" flow and the estimator simulations.

4 Estimation and control of linear perturbations

This section summarizes reports on the implementation of the estimator.

4.1 Modeling of the external disturbances

The external sources of perturbations in typical aeronautical applications can be wall roughness, acoustic waves, and freestream turbulence. When

using a linear model of the flow, the nonlinear effects can be seen as additional disturbances to the dynamic evolution.

We will assume the external disturbance forcing $d = (d_u, d_v, d_w)^T$ in (3.1) to be a zero-mean stationary white Gaussian process with auto correlation R. Our model for the covariance R of d assumes that the disturbance has a localized structure in space (i.e., the two-point correlation of the disturbance decays exponentially with distance) and that the correlations between forcing terms on different velocity components are zero. We assume a model for the covariance of the external forcing f of the form

$$R_{f_j f_k}(y, y', k_x, k_z) = l(k_x, k_z)\, \delta_{jk} \mathcal{M}^y(y, y'),$$

where

$$l(k_x, k_z) = \exp\left[-\left(\frac{k_x - k_x^0}{l_x}\right)^2 - \left(\frac{k_z - k_z^0}{l_z}\right)^2\right].$$

The model parameters k_x^0 and k_z^0 can be used to locate the peak energy of the disturbances in Fourier space, and l_x and l_z to tune the width of this peak. These parameters are specific for each flow case, e.g. for a typical TS-wave the peak energy will be at $k_x^0 = 0.3$ and $k_z^0 = 0$. The y variation of $R_{f_j f_k}$ is given by the function

$$\mathcal{M}^y(y, y') = w\left((y + y')/2\right)\, \exp\left[-\frac{(y - y')^2}{2d_y}\right]. \tag{5}$$

where the design parameter d_y governs the width of the two-point correlation of the disturbance in the wall-normal direction. The function $w(\xi)$ describes the variances at different distances from the wall. In the present simulations, the estimator is applied to disturbances inside the boundary layer, we thus use the wall-normal derivative of the mean flow,

$$w(\xi) = \frac{U'(\xi)}{U'(0)}, \tag{6}$$

so that the variance of the disturbance varies as the mean shear: greatest close to the wall and vanishing in the freestream. Other forms for $d(k_x, k_z)$ are also possible, and may be experimented in future work.

4.2 Zero mass-flux actuation

The numerical model in the DNS does not allow for net inflow, we thus have to enforce a zero-mass flux through the actuation strip by the transformation

$$\tilde{v}_0(x, z) = (v_0(x, z) + c)H(x), \tag{7}$$

where

$$c = -\frac{\displaystyle\int_z \int_x v_0(x, z)H(x)\,\mathrm{d}x\,\mathrm{d}z}{\displaystyle z_l \int_x H(x)\,\mathrm{d}x} \tag{8}$$

and

$$H(x) = S\left(\frac{x - (x_{\text{center}} - l_x^c)}{\Delta x}\right) - S\left(\frac{x - (x_{\text{center}} - l_x^c)}{\Delta x}\right). \tag{9}$$

$S(x)$ is a smooth step function rising from zero for negative x to one for $x \geq 1$ having continuous derivatives of all orders, while x_{center} denotes the center of the control interval. Parameters l_x^c and l_z^c are respectively the length and width of the control domain and Δx is the rise and fall distance of the actuation.

4.3   Optimal perturbation

The compensator performance is studied for transiently growing perturbations, also known as optimal perturbations after [17]. The spatial optimal perturbations in a Blasius boundary layer have been computed by [2] and [19]. The optimal perturbation is introduced at $x = -158.16$ and then marched forward to $x = 0$ with the technique developed in [2, 3]. The perturbation is introduced in the fringe region to give the proper inflow condition, as described in section 2.2. The perturbation is optimized to peak at $x = 237.24$. Here the local Reynolds number at the inflow is $Re = 468.34$ [3].

Figure 2 shows the energy of the uncontrolled flow, full information control and compensator control once steady state has been reached. Here the energy is defined as

$$E = \int_0^{2\pi/k_z^0} \int_0^\infty (u^2 + v^2 + w^2)\, \mathrm{d}y\, \mathrm{d}z, \tag{10}$$

where the spanwise wave number is $k_z^0 = 0.4897$. shows the Two different lengths of the control regions have been implemented. Both types of controllers for both control intervals work well at reducing the perturbation energy. In the case with a narrow control strip the perturbation energy starts to grow again since a stronger component of the growing disturbance remains. Note that the estimated flow energy does not reach the exact perturbation energy level, but in contrast to the TS-wave perturbation this does not seem to strongly affect the compensator performance.

The control signal for the full information and compensator control cases, applied in the interval $x \in [300, 750]$, are depicted in figure 3. The actuation presents a peak at the beginning of the control region and then a fast decay which levels out progressively. A similar feature is reported in [20] where control is applied over the whole domain.

5   Full information control of free-stream turbulence

Application of the full information control to transition induced by high levels of free-stream turbulence is summarized here.

5.1   Tuning of the control penalty

Several cases have been simulated. In all of them the inlet of the computational box is at $Re_{x_0} = 30000$, the dimension of the domain in the streamwise, wall-normal and spanwise direction are $900\delta_0^* \times 60\delta_0^* \times 50\delta_0^*$,
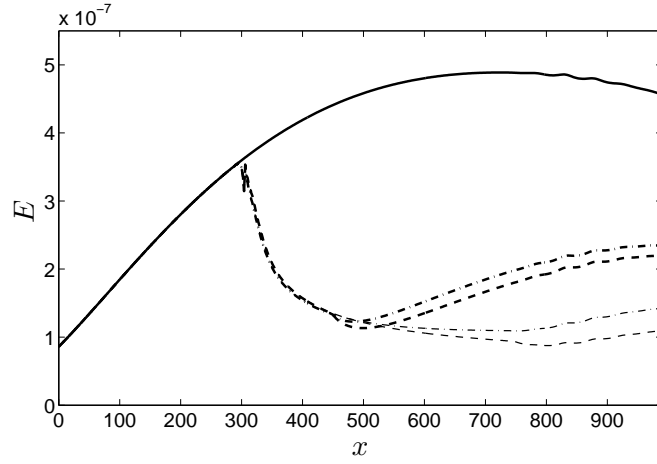
Figure 2: Spatial energy evolution of the optimal perturbation. Solid: no control. Dashed: full information control applied in region $x \in [300, 450]$. Dash-dotted: compensator control with measurement region $x_m \in [0, 300]$ and the control region $x_c \in [300, 450]$. Thin-solid: estimated flow energy. Thin-dashed: full information control applied in region $x \in [300, 725]$. Thin dash-dotted: compensator control with the measurement region $x_m \in [0, 300]$ and the control region $x_c \in [300, 725]$.
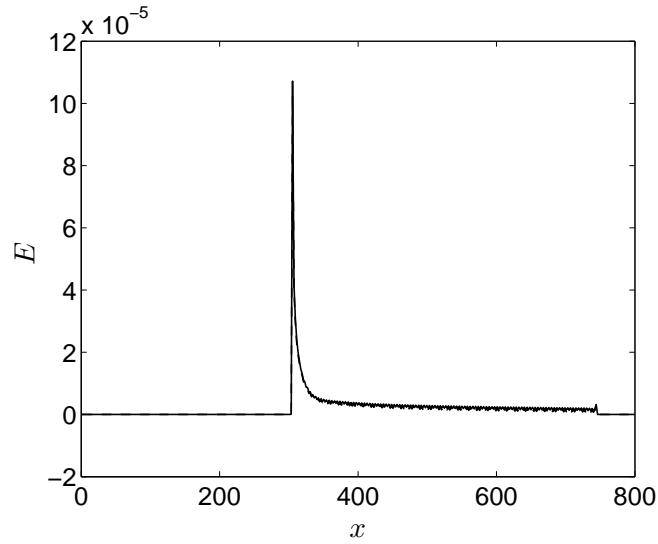

Figure 3: The control signals for the optimal disturbance case after initial transient. Dashed: full information control applied in region $x \in [300, 750]$. Dash-dotted: compensator control in domain $x \in [300, 750]$.
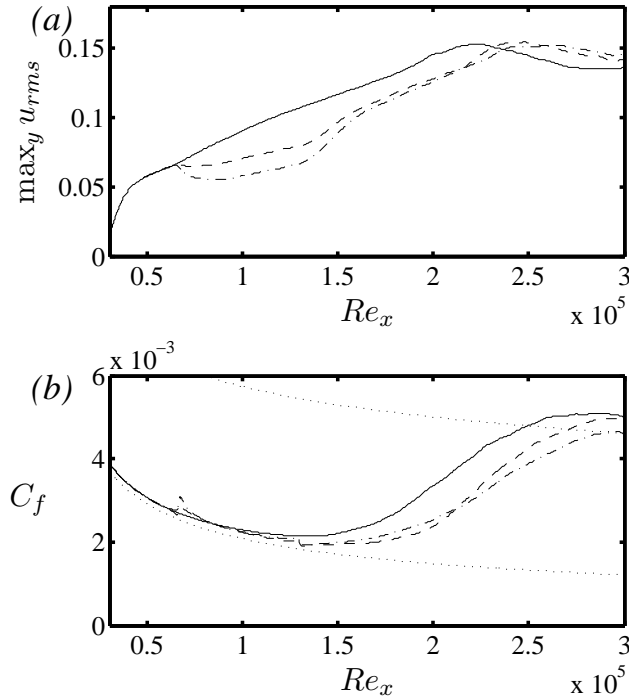
Figure 4: (*a*) Wall-normal maximum of the streamwise velocity fluctuations and (*b*) Skin friction coefficient for the simulations with $Tu = 4.7\%$. No control: ——; case *ctrl*1: - - - and case *ctrl*2: - · -.

where δ_0^* is the boundary layer thickness at x_0. $1024 \times 121 \times 72$ collocation points are used. Results are presented for a free-stream turbulence intensity $Tu = 4.7\%$. In all the simulations control is applied over the interval $Re_x \in [5.29 \times 10^4, 1.43 \times 10^5]$, and the profile used in the evaluation of the control gains is extracted at $Re_x = 9.0 \times 10^4$ for the results in this section. Two combinations of the control penalties have been used for each level of Tu, that is $l = 10^2$ and $r^2 = 1$, denoted as *ctrl*1 and $l = 10^2$ and $r^2 = 0$, denoted as *ctrl*2. For the defnition of l and r, please refer to section 3.2.1. The rms-value of the wall-normal velocity at the wall is about twice as large in the simulations with *ctrl*2 as a consequence of the lower overall control cost.

In figure 4 the results obtained by averaging in time and in the spanwise direction are presented. The wall-normal maximum of the streamwise velocity perturbation is shown in fig. 4(*a*). The values obtained without control applied are represented with a solid line, while the simulations denoted *ctrl*1 and *ctrl*2 are indicated with dashed and dashed-dotted line respectively. The growth of the u_{rms}-values inside the boundary layer is chosen since it accounts for the streak formation and growth. It can be seen that the control is able to reduce the streak growth as long as it is active and that this implies a delay of the transition location. This can be seen in Fig. 4(*b*) where the friction coefficient is displayed for the cases under consideration; also the values for a laminar and a turbulent boundary layer are reported for comparison.
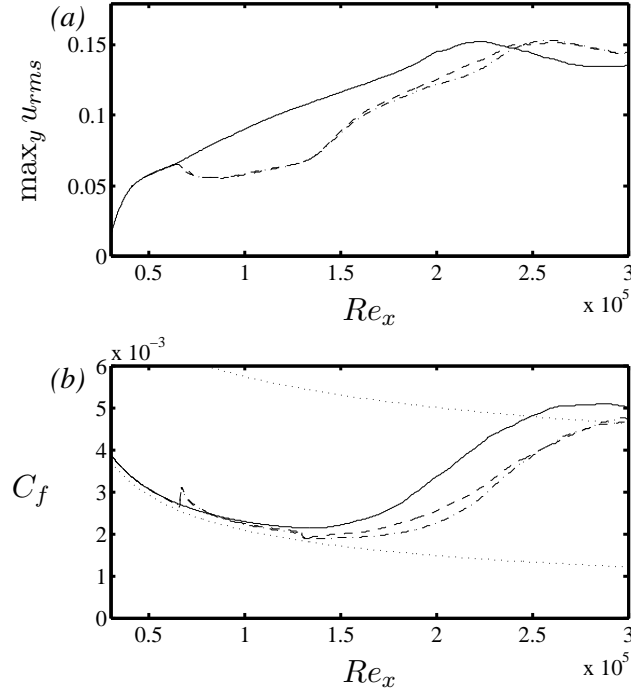
Figure 5: (*a*) Wall-normal maximum of the streamwise velocity fluctuations and (*b*) Skin friction coefficient for the simulations with $Tu = 4.7\%$. No control: ——; case *ctrl2*: - - - and case *ctrl3*: - · -.

5.2 Tuning of the extension to non-parallel flows

As discussed in section 3.2.3, the compensator problem is stated for a parallel flow. In order to extend the use of the model to a spatially evolving flow, the location where the local velocity profiles to be used in the Orr–Sommerfeld/Squire operator are taken, need to be specified. The flow is then assumed to be locally parallel around this location. Therefore, in an attempt to improve the control performance, the location of the target laminar profile is changed. Results are presented for the case, denoted as *ctrl3*, in which profile used in the evaluation of the control gains is extracted at $Re_x = 6.7 \times 10^4$, that is closer to the beginning of the control interval.

Further, to remove the assumption of zero mass-flux actuation a new implementation of the spectral code has been carried out. This enables to set the constant c in the definition of the wall-normal velocity at the wall (see eqn. 7) to zero. Thus, the control law becomes simply

$$\tilde{v}_0(x, z) = v_0(x, z) \cdot H(x), \tag{11}$$

where H, introduced in eqn.(9), limits the actuation to the chosen streamwise interval. In the new version of the numerical code the Navier-Stokes equations are solved for the velocity field $\hat{v}(x, y, z, t) = v(x, y, z, t) - \bar{v}_0(t)$, where v is the physically relevant wall-normal velocity component and $\bar{v}_0(t)$ the mass flux introduced by the actuation. The numerical implementation amounts to changes in the non-linear terms of the equation since new forcing terms arise from the interaction between $\bar{v}_0(t)$ and $\hat{v}$.
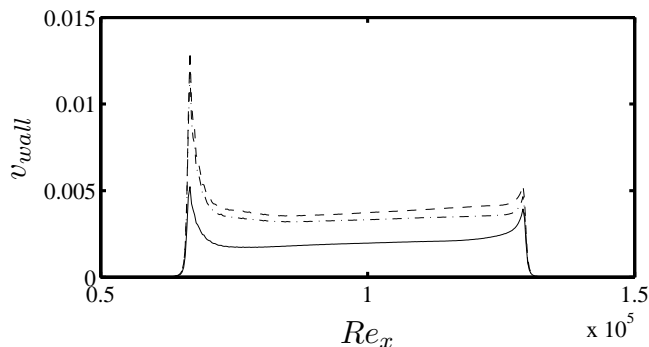
Figure 6: Wall-normal velocity fluctuations at the wall. Case $ctrl1$: ——;
case $ctrl2$: - - - and case $ctrl3$: - · -.

Simulations of actuation with non-zero mass flux were performed with
the same configuration and control kernels as in case $ctrl3$. However, once
plotted, the results differ only slightly from those of case $ctrl3$ and therefore
they will not be presented. The quantity of mass introduced by the control
turned out to be very small and therefore the improvements achieved too
small to be significative. The fact that the structures to control are spanwise
periodic and elongated in the streamwise direction can explain why, in the
mean, blowing and suction balance to give an almost zero mean mass flux at
the wall. However, the possibility of applying control without the constraint
of zero mass flux will be certainly exploited for other types of disturbance.

The comparison of the results obtained with the control $ctrl2$ and $ctrl3$
is displayed in figure 5, where both the wall-normal maximum of the stream-
wise velocity fluctuations and the skin friction coefficient are shown. For the
control based on the most-upstream local profile, a smaller growth of the
perturbations is observed downstream of the actuation region. The rms-
value of the wall-normal velocity at the wall, the energy spent at the wall,
is depicted in figure 6 for the three control laws under considerations. As
mentioned above, the control effort is the smallest for case $ctrl1$ owing to
the higher control cost. The energy spent by the control $ctrl3$ is lower than
that needed by $ctrl2$, so that the diminished control cost should be added to
the small improvements in terms of transition delay (see fig. 5) in the global
comparison between the two cases.

From the results presented, one can conclude that the control is able to
delay/stop the growth of the streaks, which are responsible, through their
secondary instabilities, of the considered bypass transition scenario. How-
ever, it is also observed that, if too strong localized blowing is applied,
turbulent spots are induced by local instabilities due to wall-normal inflec-
tional profiles. An improvement of the transition delay can therefore be
achieved by applying control over a longer domain.

6 Large-eddy simulation of control of free-stream turbulence

The main new work during the first part of PHASE 3 is presented in this section.

As noted above, to fully resolve transition in boundary layers exposed to free-stream turbulence demands large computational resources, in particular when combined with control and estimation. Therefore, in order to perform a complete study of the control problem it was decided to use large-eddy simulation (LES, [24]) to model the evolution of the smallest spatial scales during transition and turbulence. Such a modeling approach allows to more easily test and validate different control strategies and carry out parameter studies. Furthermore, the LES formulation itself can be regarded as a model-reduction tool in the estimation problem, i.e. the estimator can run an LES whereas a full DNS is computing the real (physical) setup.

6.1 Large-eddy simulation of transitional and turbulent flows

When using LES, the turbulent vortices (eddies) above a certain size are completely resolved on the numerical grid, whereas the effect of the smaller scales on the larger ones needs to be modelled. The idea behind this scale separation is that the smaller eddies are more homogeneous and isotropic than the large ones and depend little on the specific flow situation, whereas the energy-carrying large-scale vortices are strongly affected by the particular flow conditions (geometry, inflow, etc.), see e.g. [21].

It is expected that LES will play a major role in the future for prediction and analysis of certain complex turbulent flows in which a representation of unsteady turbulent fluctuations is important, such as laminar-turbulent transition, large-scale flow separation in aerodynamics, coupled fluid-structure interaction, turbulent flow control, aeroacoustics and turbulent combustion.

The self similarity of the small scales is often supposed to allow an easier modeling. Since for LES not all scales have to be resolved on the computational grid, only a fraction of the computational cost compared to fully resolved DNS (typically of order 1%) is required. There are two major steps involved in the LES analysis: filtering and subgrid-scale modeling (SGS). Considerable research effort has recently been devoted to the development of SGS models of velocity estimation or deconvolution type, see e.g. the review by [22] and to models based on a multiscale approach [25, 26].

The use of large-eddy simulations (LES) to predict transitional and turbulent flow is appealing as they promise to provide accurate results at greatly reduced computational cost in comparison with DNS. A suitable SGS is important since the transitional flows have complex interactions between the base flow and various instability modes. The specific case of forced K-type transition in channel flow has been simulated successfully using ADM and related modeling strategies in [21].

To visualize the LES methodology, we start with the Navier-Stokes equa-

tions:

$$\frac{\partial u_i}{\partial t} + \frac{\partial u_i u_j}{\partial x_j} = -\frac{\partial p}{\partial x_i} + \frac{1}{Re}\frac{\partial^2 u_i}{\partial x_j \partial x_j} \tag{12}$$

$$\frac{\partial u_i}{\partial x_i} = 0 \tag{13}$$

In the traditional LES approach, equations (12) and (13) are spatially filtered with a low-pass filter G^P (*primary LES filter*) with some filter width Δ. The primary low-pass filtered velocity is given by the convolution

$$\bar{u}_i(x) := G^P * u_i := \int_\Gamma G^P(x, x', \Delta) u_i(x') dx' \tag{14}$$

The filtering operation yields the LES equations

$$\frac{\partial \bar{u}_i}{\partial t} + \frac{\partial \bar{u}_i \bar{u}_j}{\partial x_j} = -\frac{\partial \bar{p}}{\partial x_i} - \frac{\partial \tau_{ij}}{\partial x_j} + \frac{1}{Re}\frac{\partial^2 \bar{u}_i}{\partial x_j \partial x_j} \tag{15}$$

$$\frac{\partial \bar{u}_i}{\partial x_i} = 0 \tag{16}$$

The LES equations govern the evolution of the large, energy-carrying scales of motion. The effect of the non-resolved small scales enters in equation (15) through the subgrid-scale (SGS) term, $\tau_{ij} := \overline{u_i u_j} - \bar{u}_i \bar{u}_j$ which is not closed since $\overline{u_i u_j}$ cannot be obtained from the filtered quantities $\bar{u}_i$ alone. τ_{ij} must thus be modelled by an appropriate SGS model.

The SGS models which are used in this simulations are the relaxation-term model (ADM-RT) and the high-pass filtered (HPF) eddy-viscosity models. Here, we will give a short description of the ADM-RT model which is a modification of the approximate deconvolution model (ADM) specifically designed for use with high-order numerical schemes, such as spectral methods. This model was found to be suitable for LES of transitional and turbulent flows [21]. The nonlinear terms are evaluated as

$$\frac{\partial \bar{u}_i \bar{u}_j}{\partial x_j} \; , \tag{17}$$

i.e. no modification of the nonlinear terms as used in e.g. the scale-similarity model was found necessary. The subgrid-scale term for ADM-RT model to close equation (15) can be written as follows

$$\frac{\partial \tau_{ij}}{\partial x_j} = \mathcal{X}(I - Q_N * G) * \bar{u}_i \; = \mathcal{X}(I - G)^{N+1} * \bar{u}_i = \mathcal{X}H_N * \bar{u}_i \tag{18}$$

with the definition on an approximate inverse of the filter G,

$$Q_N = \sum_{\nu=0}^{N}(1 - G)^\nu \approx G^{-1}.$$

The combined filter $H_N = I - Q_N * G$ is a high-order high-pass filter. This way, only the smallest resolved scales present in the simulation are affected by the model contributions whereas the larger scales are virtually

unaffected and can develop as in a direct simulation. The relaxation term $-\mathcal{X}(I - Q_N * G) = -\mathcal{X}H_N * \bar{u}_i$ provides the necessary drain of energy out of the coarsely discretized system. Note that the LES filter operation (14) is the implicit grid filter, i.e. no explicit filtering of the flow field is performed.

The complete LES equations for the ADM-RT model combining equations (15) and (18) are

$$\frac{\partial \bar{u}_i}{\partial t} + \frac{\partial \bar{u}_i \bar{u}_j}{\partial x_j} = -\frac{\partial \bar{p}}{\partial x_i} + \frac{1}{Re}\frac{\partial^2 \bar{u}_i}{\partial x_j \partial x_j} - \mathcal{X}H_N * \bar{u}_i \; . \qquad (19)$$

The incompressible LES equations (19) are discretized with the same method as in the DNS implementation by a fully spectral method with Fourier representation in the periodic wall-parallel directions and by a Chebyshev tau method in the wall-normal direction. Time advancement is achieved by a semi-implicit low-storage second-order Runge-Kutta/Crank-Nicolson scheme.

6.2 Large-eddy simulation of bypass transition

Schlatter and Brandt [23] showed recently that using large-eddy simulation (LES) applying the ADM-RT model one can correctly reproduce bypass transition, as shown in the following two figures.

For modeling of bypass transition, the optimized fully-spectral numerical simulation code used for the recent direct simulations of bypass transition [12] has been extended with a number of SGS models capable of predicting transitional flows, i.e. models proposed in Refs. [27, 26]. Due to the use of Fourier-spectral numerical discretization, the interaction of the LES methodology and the non-periodic boundary treatment needed for the simulation of spatially evolving flows (fringe method) deserves special attention and has been validated separately [21]. The grid resolution could be reduced to less than 10% of the corresponding DNS resolution [12].
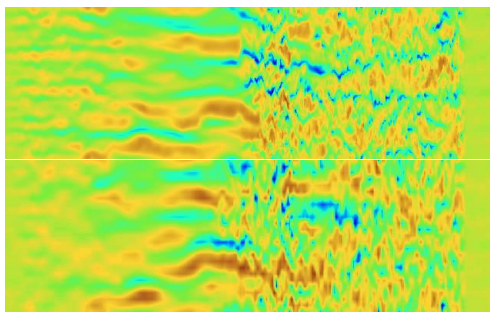

Figure 7: Contours of the instantaneous streamwise velocity component in a plane parallel to the solid wall for bypass transition. *Left:* Direct numerical simulation (DNS). *Right:* Large-eddy simulation (LES) using less than 10% of the resolution of the DNS.

Figure 8 shows the evolution of the skin friction along the plate. As can be seen, the underresolved no-model LES (coarse DNS) undergoes transition much too early and thus leads to an inaccurate prediction of the transition scenario. Using an SGS model, transition can be predicted much more
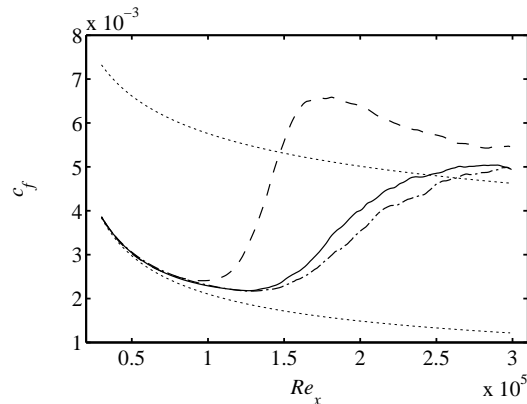
Figure 8: Evolution of the skin friction coefficient c_f along the streamwise direction Re_x of the flat plate. $-\cdot-$ Fully resolved DNS, ——— large-eddy simulation using ADM-RT, $----$ no-model LES (coarse-grid DNS). $\cdots\cdots$ empirial correlations for laminar and turbulent boundary-layer flow (from [23]).

accurately, as seen in the comparison of the ADM-RT model and the DNS. Note that the numerical resolution (and thus the computational effort) for the DNS ist more than 10 times higher than for the LES.

An instantaneous visualization of the streamwise velocity component in a plane close to the wall is shown in figure 7. It is evident that in both the DNS and LES the streamwise elongated structures ("streaks"), which are characteristic for bypass transition, appear. Moreover, the visual appearance of these structures is similar between DNS and LES. The breakdown to turbulence, indicated by a strongly increased chaotic motion, occurs at a similar downstream position for both LES and DNS.

With these encouraging results, we can go further and apply the zero-mass flux control at the wall to the LES calculations using the optimal control theory described in chapter 3 above.

6.3 Large-eddy simulation of full-information optimal control

Having shown that LES allows to obtain reasonably accurate results for bypass transition compared to a fully-resolved DNS, we proceed to perform a parameter study to investigate the effect of different control parameters. Since no large differences were found between the zero-mass flux control and the non-zero mass-flux control in our DNS study, we implement the zero-mass flux control into the LES code and compare the results in a first validation step with the DNS implementations (results presented as *ctrl4*, same configuration as *ctrl3*). Furthermore, the effect of applying the zero mass-flux control for a longer streamwise domain is also considered (case denoted *ctrl5*).

For the same box size, the resolution used for the LES simulations is $256 \times 121 \times 36$, which is considerably lower than the one adopted in the direct numerical simulation. The parameters for the free-stream turbulence intensity and its length scale, and also the control region specifications used
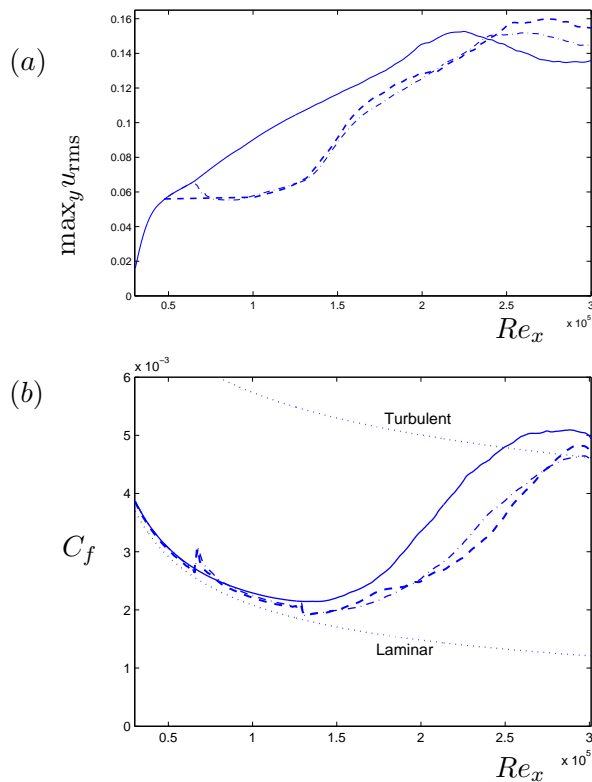
Figure 9: (a) Wall-normal maximum u_{rms}, (b) skin-friction coefficient. —— $ctrl1$; $-\cdot-$ $ctrl3$; $----$ $ctrl4$.

here are the same as in the DNS, case $ctrl3$. The results are presented for free-stream turbulence intensity $Tu = 4.7\%$, which was studied in detail in [12]. In the LES applying the ADM-RT model with zero-mass flux control (denoted as $ctrl4$) the active control is applied over the streamwise interval $Re_x \in [5.29 \times 10^4, 1.43 \times 10^5]$. For the zero-mass flux control with a longer control region (denoted as Case6) control is applied over the interval $Re_x \in [5.27 \times 10^4, 2.18 \times 10^5]$. The profile used in the evaluation of the control gains is extracted at $Re_x = 6.7 \times 10^4$, and the control penalties are $\ell = 10^2$ and $r^2 = 0$, for both case.

In figure 9(a) the wall-normal maximum of the streamwise velocity per-turbation is shown. It can be seen that the zero-mass flux control using LES gives results which are similar to the corresponding data obtained by direct numerical simulations ($ctrl3$). We can therefore conclude that LES is able to correctly reproduce the effect of the non-resolved subgrid scales even in the presence of active blowing and suction at the lower wall. Moreover, the controller is able to generate similar control signals as in the DNS. This is an important results since it allows to perform the aforementioned param-eter studies to be performed based on an LES grid, which is substantially coarser than the DNS grid. From a physical point of view, the control is able to reduce the streak growth as long as it is active and this implies a delay of transition location. The transition delay is more apparant in figure 9(b) where the skin-friction coefficient is displayed. Since the LES method
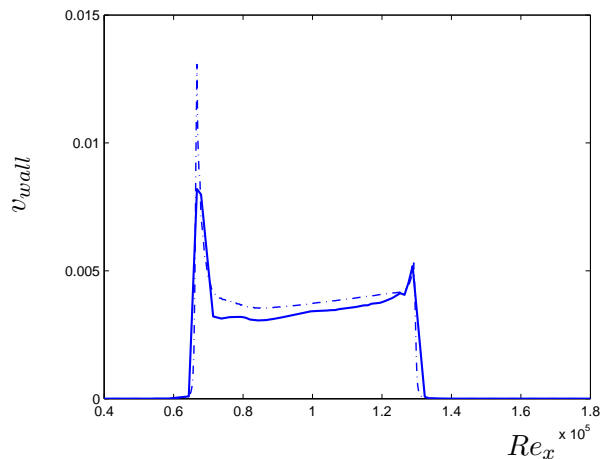
Figure 10: The velocity at the wall which represents the control signal. $-\cdot-ctrl3$; $----ctrl4$.

only accounts the effect of larger scales slight differences compared with the DNS simulations are visible. This is however more than compensated by the considerable reduction in computational cost necessary for the LES.

The fluctuations of the wall-normal velocity at the wall which corresponds to the control signal and thus the energy spent by the control actuation, is diplayed in figure 10. The energy necessary for the control $ctrl4$ is lower than that needed by $ctrl3$, which is due to the fact that the control is only acting on a larger scale.

In figure 11 results for case $ctrl5$ are shown. It can be inferred from the figure $11(a)$ that with a longer control domain, it is possible to reduce the streak growth even more than with a shorter one. The effect of the control is more pronounced when considering the skin-friction coefficient C_f as shown in figure $11(b)$. By comparing the two plots it can be deduced that the large values of streamwise velocity fluctuations towards the end of the computational domain are not associated with a fully turbulent flow, i.e. the transition delay was able to move the transition point outside the computational domain. Further calculations with increased domain length are planned.

From the results presented so far, one can conclude that it is well possible to use large-eddy simulation, and in particular the ADM-RT model to study the performance of optimal control in bypass transition on a flat-plate boundary layer. The results are indeed in good agreement with the direct numerical simulation (DNS). In LES only the effect of the large scales is accounted for, therefore, it implies a significantly lower computational effort.
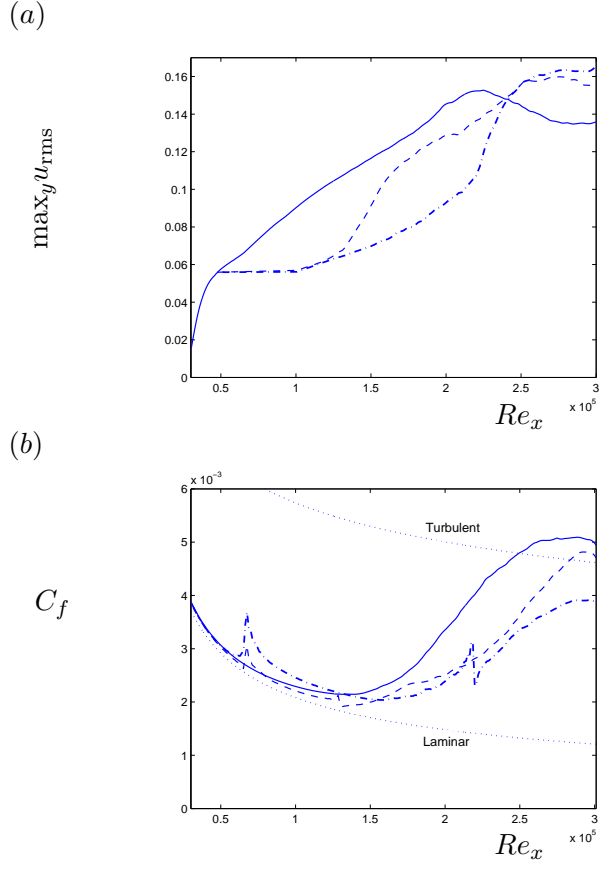
(a)

(b)

Figure 11: (a) Wall-normal maximum u_{rms}, (b) skin-friction coefficient. —— $ctrl1$; - - - - $ctrl4$; - · - $ctrl5$.
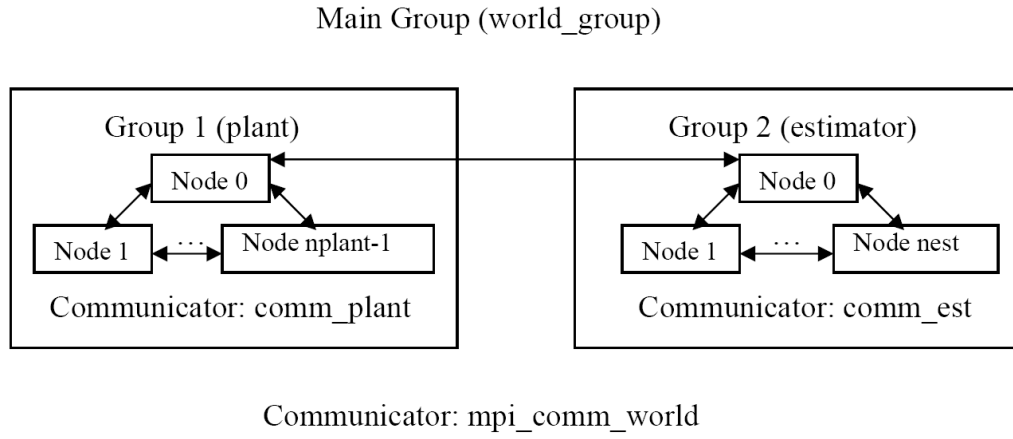
Main Group (world_group)

Communicator: mpi_comm_world

Figure 12: Sketch of the parallel implementation of plant and estimator.

7 Estimation and compensation of free-stream turbulence

7.1 Implementation of compensator

As mentioned above, the present numerical experiments of feedback control in boundary layer flows are based on the simultaneous simulation of two velocity fields: the plant representing the actual physical flow where blowing/suction needs to be applied and wall measurements are taken, and the estimator where the velocity field is reconstructed based on the measurements in order to compute the control law. From a practical point of view, this imply the need to run two distinct processes, plant and estimator, which need to communicate data (measurements and control law) during the execution time. To be able to efficiently run the present simulations on the available commodity clusters without contraints on the two processes, thus allowing different resolutions and box sizes, a novel parallel implementation of the spectral code is done. The coupling between the two codes is achieved by letting each code run in its own separate address space and communication occurs via standard MPI message passing on the global level. A sketch of the implementation is reported in figure 12.

7.2 Results

Large-eddy simulations of the estimator and compensator have been performed. The flow configurations initially adopted is the same as in the previous sections, i.e. inflow $Re_x = 30000$, box dimensions $1000\times60\times50$ with resolution $256\times121\times36$ and free-stream turbulence intensity $Tu = 4.7\%$. The estimation forcing is applied in the range $Re_x \in [3.8 \times 10^4, 1.28 \times 10^5]$, with reference base flow at $Re_x = 8.3 \times 10^4$. Careful tuning of the sensor noise of the estimation kernels was necessary in order to obtain a satisfactory estimation: the elongated streamwise velocity structures can be qualitatively and quantitatively reproduced in the estimator simulation. Note, however, that the control can only be applied downstream of the estimation region. For the high levels of free-stream turbulence considered so far, this amounts to applying the wall blowing/suction to flow structures which are already transitional. Therefore, it was decided to decrease the intensity of the incoming free-stream disturbances to $Tu = 3\%$ and double the length of the simulation domain to $2000\delta_0^*$ at the same resolution (now 512 grid points in the streamwise direction).

In the simulations of the compensator, estimation is applied at $Re_x \in [4.5 \times 10^4, 1.95 \times 10^5]$ with reference boundary layer profile extracted at $Re_x = 1.2 \times 10^5$, whereas blowing and suction at the wall is active in the region $Re_x \in [1.8 \times 10^5, 3.0 \times 10^5]$ targeting the flow at $Re_x = 2.4 \times 10^5$. Results on the estimation at this lower free-stream turbulence intensity are presented in figures 13 and 14. Instantaneous flow configurations from the plant (uncontrolled flow) and the estimated velocity field in a wall-parallel plane at distance from the wall $y = 2$ are displayed in figure 13 in terms of the streamwise veocity perturbation. It can be seen that in the estimation region and just downstream of it the main streaky structures are well predicted.
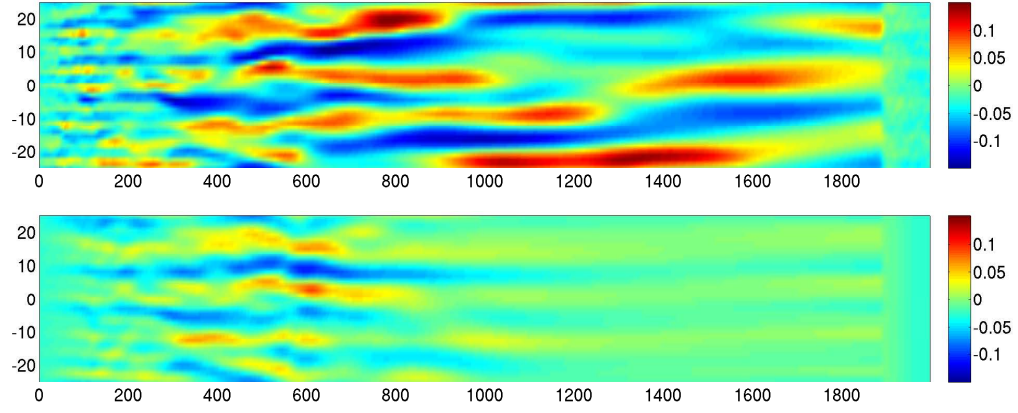
Figure 13: Instantaneous streamwise velocity perturbation in a wall parallel plane, $y = 2$. Top: plant. Bottom: estimated field.
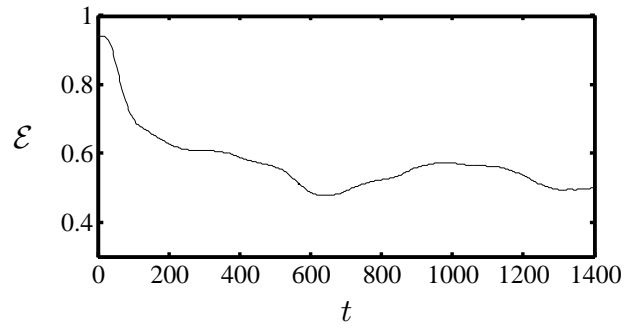

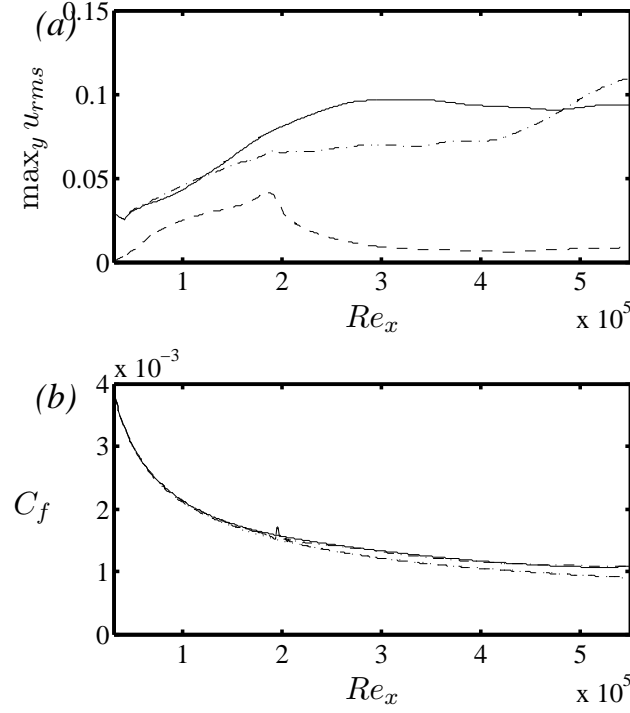Figure 14: Time evolution of the estimation error $\mathcal{E}$. See definition of $\mathcal{E}$ in the text.

Figure 15: (*a*) Wall-normal maximum of the streamwise velocity fluctuations and (*b*) Skin friction coefficient for the simulations with $Tu = 3\%$. No control: ——; estimator: - - - and compensator: - · -.

Quantitave data on the difference between the plant and the reconstructed field are presented in figure 14. The error is measured by the difference in streamwise perturbation velocity between the plant and estimator normalised by the local perturbation intensity averaged in the spanwise direction.

$$\mathcal{E} = \frac{1}{L_{es}} \int_{x1}^{x2} \frac{u'_{pl}(x, 2, z) - u'_{es}(x, 2, z)}{\langle u'_{pl}(x) \rangle} dx \ ,$$

where

$$\langle u'_{pl}(x) \rangle = \frac{1}{L_z} \int u'_{pl}(x, 2, z) dz \ .$$

$\mathcal{E}$ can therefore be seen as the relative error in the streak intensity averaged over the estimation length. The figure shows that after an initial transient an average error of about 50% is attained. The results of the compensator simulation are shown in figure 15. In figure 15(*a*) the wall-normal maximum of the streamwise velocity perturbation is reported in order to quantify the streak growth in the uncontrolled case (solid line), in the estimator, i.e. in the field the reconstructed from the wall measurements (dashed line) and in the compensator where control based on the estimated field is applied to the flow where measurements were taken (dash-dotted line). A lower streak intensity, reaching a value of about 10%, is observed at this lower level of external perturbation if compared with the results from the previous sections. In average, the estimated streaky structures are of about

half the intensity of those in the uncontrolled case. However, the averaged values reported here are likely to mask the fact that locally the most intense structures are better reproduced, the same being valid also for the error $\mathcal{E}$ in figure 14. From $Re_x = 2 \times 10^5$, where full information control is applied also in the estimated field, a rapid decay of the streaks can be oberved. The application of control from the estimated field in the plant leads to a quenching of the streak growth. However, as observed in the case of full information control, a rapid amplification of the perturbation occurs downstream of the control region, in this case leading to values higher than those observed in the uncontrolled case. In figure $15(b)$ the skin friction coefficient pertaining to the same three velocity fields is considered. Owing to the weak perturbation intensity in the estimated field, the values are closer to pertaining to the laminar boundary layer flow. The skin friction measured in the compensator simulation is very close to that attained in the uncontrolled case.

The performance of the compensator can certainly be improved. Future work would also need to consider the direct numerical simulation of the plant and large-eddy simulation in the estimated field.

8   Conclusions and future work

This concludes the comprehensive report on PHASE 3 of this project. We have archived the main goals of this study, namely to apply LQR feedback control to laminar turbulent transition in boundary layers subjected to free-stream turbulence. We have seen that the control works fine, and that the estimation is adequate, but that there is possibilities to improve the combined effort of the compensator. This is possibly something to continue to work on in the future. This being said, we should mention that this is the first test of modern optimal feedback control to such a complicated flow with so many degrees of freedom, and as such it is certainly a success.

Possible continuation of this project has been suggested in a white paper produced some months ago. Despite the recent progresses, two aspects of the control problem have been identified as crucial in order to extend the methodology to more complex flows and achieve further improvement. They are

- the need to go beyond the assumption of parallel base flows

- model reduction to significantly decrease the cost of the estimation and thus of the computation of the control gains.

Therefore, the aim of a possible continuation of our EOARD/AFOSR project is to develop the theory and tools to apply feedback control in highly non-parallel flow configurations.

References

[1] M. Matsubara and P. H. Alfredsson, "Disturbance growth in boundary layers subjected to free stream turbulence," *J. Fluid. Mech.*, vol. 430, pp. 149–168, 2001.

[2] P. Andersson, M. Berggren, and D. S. Henningson, "Optimal disturbances and bypass transition in boundary layers," *Phys. Fluids*, vol. 11, pp. 134–150, 1999.

[3] P. Andersson,,L. Brandt,A. Bottaro and D. S. Henningson, "On the breakdown of boundary layer streaks," *J. Fluid Mech.*, vol. 428, pp. 29–60, 2001.

[4] L. Brandt, P. Schlatter, and D. S. Henningson, "Numerical simulations of transition in a boundary layer under free-stream turbulence." in *Advances in Turbulence IX, Proc. of the Ninth European Turbulence Conference*, P. E. H. I. Castro and T. G. Thomas, Eds., CIMNE, 2002, pp. 17–20.

[5] L. Brandt, "Numerical studies of bypass transition in the Blasius boundary layer," Doctoral thesis, Royal Institute of Technology, Stockholm, Sweden, 2003.

[6] A. Lundbladh, S. Berlin, M. Skote, C. Hildings, J. Choi, J. Kim, and D. S. Henningson, "An efficient spectral method for simulation of incompressible flow over a flat plate," KTH, Department of Mechanics, Stockholm, Technical Report KTH/MEK/TR–99/11–SE, 1999.

[7] F. P. Bertolotti, T. Herbert, and P. R. Spalart, "Linear and nonlinear stability of the Blasius boundary layer," *J. Fluid Mech.*, vol. 242, pp. 441–474, 1992.

[8] J. Nordström, N. Nordin, and D. S. Henningson, "The fringe region technique and the Fourier method used in the direct numerical simulation of spatially evolving viscous flows," *SIAM J. Sci. Comp.*, vol. 20, pp. 1365–1393, 1999.

[9] R. G. Jacobs and P. A. Durbin, "Simulations of bypass transition," *J. Fluid Mech.*, vol. 428, pp. 185–212, 2001.

[10] R. S. Rogallo, "Numerical experiments in homogeneous turbulence," NASA, Tech. Rep. Tech. Memo. 81315, 1981.

[11] C. E. Grosch and H. Salwen, "The continuous spectrum of the Orr-Sommerfeld equation. Part 1.The spectrum and the eigenfunctions." *J. Fluid Mech.*, vol. 87, pp. 33–54, 1978.

[12] L. Brandt, P. Schlatter, and D. S. Henningson, "Transition in boundary layers subject to free-stream turbulence," *J. Fluid Mech.*, vol. 517, pp. 167–198, 2004.

[13] L. Brandt and D. S. Henningson, "Transition of streamwise streaks in zero-pressure-gradient boundary layers," *J. Fluid Mech.*, vol. 472, pp. 229–262, 2002.

[14] M. Asai, M. Minagawa, and M. Nishioka, "The instability and breakdown of a near-wall low-speed streak," *J. Fluid Mech.*, vol. 455, pp. 289–314, 2002.

[15] O. Levin, "Stability analysis and transition prediction of wall-bounded flows," Licentiate thesis, Royal Institute of Technology, Stockholm.

[16] M. Högberg, "Optimal Control of Boundary Layer Transition," Doctoral thesis, Royal Institute of Technology, Department of Mechanics, Stockholm, Sweden.

[17] K. M. Butker and B. F. Farrell, " Three-dimensional optimal perturbations in viscous shear flow," *Phys. Fluids*, vol. 4, pp. 1637–1650, 1992.

[18] M. Högberg and D. S. Henningson. "Linear optimal control applied to instabilities in spatially developing boundary layers." *J.* Fluid Mech., 470, pp.151–179, 2002.

[19] P. Luchini, "Reynolds-number-independent instability of the boundary layer over a flat surface: Optimal Perturbations," *J. Fluid Mech.*, vol. 404, pp. 289–309, 2000.

[20] P. Cathalifaud and P. Luchini, "Algebraic growth in boundary layers: Optimal control by blowing and suction at the wall," *Eur. J. Mech./B Fluids*, vol. 19, pp. 469–490, 2000.

[21] P. Schlatter, "Large-eddy simulations of transition and turbulence in wall-bounded shear flows. *Doctoral Thesis*, ETH Zurich, Switzerland, 2005.

[22] J. A. Domaradzki and N. A. Adams, "Direct modelling of subgrid scales of turbulence in large eddy simulations".*J. Turbulence,***3**, 2002.

[23] P. Schlatter and L. Brandt, "LES of Bypass Transition," *Whither Turbulence Prediction and Control Conference*, Seoul, Korea, March 26-29,2006.

[24] P. Sagaut. *Large Eddy Simulation for Incompressible Flows.* Springer, third edition, 2005.

[25] T. J. R. Hughes, L. Mazzei, and K. E. Jansen. Large eddy simulation and the variational multiscale method. *Comput. Visual. Sci.*, 3:47–59, 2000.

[26] S. Stolz, P. Schlatter, and L. Kleiser. High-pass filtered eddy-viscosity models for large-eddy simulations of transitional and turbulent flow. *Phys. Fluids*, 17:065103, 2005.

[27] P. Schlatter, S. Stolz, and L. Kleiser. LES of transitional flows using the approximate deconvolution model. *Int. J. Heat Fluid Flow*, 25(3):549–558, 2004.